Influence of sub-nanosecond time of flight resolution for online range verification in proton therapy using the line-cone reconstruction in Compton imaging

Jayde Livingstone, Denis Dauvergne, A. Etxebeste, Mattia Fontana, Marie-Laure Gallin-Martel, Brent Huisman, Jean Michel Létang, Sara Marcatili, David Sarrut, Etienne Testa

To cite this version:

Jayde Livingstone, Denis Dauvergne, A. Etxebeste, Mattia Fontana, Marie-Laure Gallin-Martel, et al.. Influence of sub-nanosecond time of flight resolution for online range verification in proton therapy using the line-cone reconstruction in Compton imaging. Physics in Medicine and Biology, 2021, 66, pp.125012. 10.1088/1361-6560/ac03cb . hal-03257804

HAL Id: hal-03257804
https://hal.science/hal-03257804

Submitted on 14 Jun 2021

Physics in Medicine & Biology

ACCEPTED MANUSCRIPT

Influence of sub-nanosecond time of flight resolution for online range verification in proton therapy using the line-cone reconstruction in Compton imaging

To cite this article before publication: Jayde Livingstone *et al* 2021 *Phys. Med. Biol.* in press https://doi.org/10.1088/1361-6560/ac03cb

Manuscript version: Accepted Manuscript

Accepted Manuscript is “the version of the article accepted for publication including all changes made as a result of the peer review process, and which may also include the addition to the article by IOP Publishing of a header, an article ID, a cover sheet and/or an ‘Accepted Manuscript’ watermark, but excluding any other editing, typesetting or other changes made by IOP Publishing and/or its licensors”

This Accepted Manuscript is **© 2021 Institute of Physics and Engineering in Medicine**.

During the embargo period (the 12 month period from the publication of the Version of Record of this article), the Accepted Manuscript is fully protected by copyright and cannot be reused or reposted elsewhere.
As the Version of Record of this article is going to be / has been published on a subscription basis, this Accepted Manuscript is available for reuse under a CC BY-NC-ND 3.0 licence after the 12 month embargo period.

After the embargo period, everyone is permitted to use copy and redistribute this article for non-commercial purposes only, provided that they adhere to all the terms of the licence https://creativecommons.org/licences/by-nc-nd/3.0

Although reasonable endeavours have been taken to obtain all necessary permissions from third parties to include their copyrighted content within this article, their full citation and copyright line may not be present in this Accepted Manuscript version. Before using any content from this article, please refer to the Version of Record on IOPscience once published for full citation and copyright details, as permissions will likely be required. All third party content is fully copyright protected, unless specifically stated otherwise in the figure caption in the Version of Record.

View the article online for updates and enhancements.

This content was downloaded from IP address 134.214.188.172 on 14/06/2021 at 06:53

Influence of sub-nanosecond time of flight resolution for online range verification in proton therapy using the line-cone reconstruction in Compton imaging

Jayde Livingstone[1,2], **Denis Dauvergne**[2], **Ane Etxebeste**[3], **Mattia Fontana**[1], **Marie-Laure Gallin-Martel**[2], **Brent Huisman**[3], **Jean Michel Létang**[3], **Sara Marcatili**[2], **David Sarrut**[3] and **Étienne Testa**[2]

[1]Univ Lyon, Université Claude Bernard Lyon 1, CNRS/IN2P3, Institut de Physique des 2 Infinis, 69622 Villeurbanne, France

[2]Université Grenoble Alpes, CNRS/IN2P3, Laboratoire de Physique Subatomique et de Cosmologie, 38026 Grenoble, France

[3]University of Lyon, INSA-Lyon, Université Claude Bernard Lyon 1, UJM-Saint Etienne, CNRS, Inserm, CREATIS UMR 5220, U1206, F-69373 Lyon, France

E-mail: `Jayde.Livingstone@univ-grenoble-alpes.fr`

June 2020

Abstract. Online ion range monitoring in hadron therapy can be performed via detection of secondary radiation, such as prompt γ-rays, emitted during treatment. The prompt γ emission profile is correlated with the ion depth-dose profile and can be reconstructed via Compton imaging. The line-cone reconstruction, using the intersection between the primary beam trajectory and the cone reconstructed via a Compton camera, requires negligible computation time compared to iterative algorithms. A recent report hypothesised that time of flight (TOF) based discrimination could improve the precision of the γ fall-off position measured via line-cone reconstruction, where TOF comprises both the proton transit time from the phantom entrance until γ emission, and the flight time of the γ-ray to the detector. The aim of this study was to implement such a method and investigate the influence of temporal resolution on the precision of the fall-off position. Monte Carlo simulations of a 160 MeV proton beam incident on a homogeneous PMMA phantom were performed using GATE. The Compton camera consisted of a silicon-based scatterer and CeBr$_3$ scintillator absorber. The temporal resolution of the detection system (absorber + beam trigger) was varied between 0.1 and 1.3 ns RMS and a TOF-based discrimination method applied to eliminate unlikely solution(s) from the line-cone reconstruction. The fall-off position was obtained for varying temporal resolutions and its precision obtained from its shift across 100 independent γ emission profiles compared to a high statistics reference profile. The optimal temporal resolution for the given camera geometry and 10^8 primary protons was 0.2 ns where a precision of 2.30 ± 0.15 mm (1σ) on the fall-off position was found. This precision is comparable to current state-of-the-art Compton imaging using iterative reconstruction methods or 1D imaging with mechanically collimated devices, and satisfies the requirement of being smaller than the clinical safety margins.

Keywords: Hadron therapy, proton therapy, Compton imaging, Compton camera, time of flight, online verification
Submitted to: *Phys. Med. Biol.*

1. Introduction

Hadron therapy involves the use of light positively charged ions in the treatment of malignant tumours. The depth-dose profile of ions, characterised by a relatively low entrance dose, well defined range and highly localised dose deposition at the end of the particle track, makes ions an interesting choice in radiotherapy. In theory, the sharp distal fall-off following the Bragg peak could be used to define the edge of the treatment field where an organ at risk lies in close proximity to the tumour, sparing the organ at risk as all of the particles are stopped inside the tumour. However, due to uncertainties either in the calculation of the ion stopping power at the treatment planning stage, or in the delivery of the treatment due to mispositioning or changes in patient/tumour morphology, this practice is almost never carried out in treatment centres (Knopf *et al.*, 2013). Instead, to avoid important under-dosage of the tumour and/or over-dosage of the normal tissue downstream of the tumour, margins of [2.5–3]%+[2–3] mm are typically applied to the target volume (Paganetti, 2012), which for deep-seated tumours can be of the order of a centimeter.

Minimising the ion-range uncertainty would allow the favourable dose deposition characteristics of ions to be exploited. Numerous methods for reducing the ion-range uncertainty, either at the treatment planning stage or during the treatment via online monitoring, have been investigated and discussed in the literature (Knopf *et al.*, 2013; Parodi *et al.*, 2018). Amongst the methods of online monitoring is the detection of secondary radiation emitted as a result of the interaction of the ion beam with the patient. Nuclear interactions involving incident ions and the patient often result in the almost instantaneous emission of prompt γ rays. The γ emission vertices correspond to locations of nuclear reactions and are correlated with the primary ion range, thus making it possible to use longitudinal profiles obtained via prompt γ imaging (PGI) as a tool to retrieve dosimetric quantities related to the ion range (e.g., Bragg peak or fall-off position) (Knopf *et al.*, 2013; Krimmer *et al.*, 2018). PGI devices typically require collimation, either mechanical or electronic, to provide information about the incidence direction of the prompt γ detected. Of the different mechanical collimation geometries that have been tested, the knife-edge slit (KES) is perhaps the most advanced, achieving a standard deviation of 1–2 mm on the range estimation of a 160 MeV proton pencil beam (10^8 particles) incident on a PMMA phantom (Smeets *et al.*, 2012) and proven performance in a clinical setting (Perali *et al.*, 2014; Richter *et al.*, 2016; Verburg *et al.*, 2020; Xie *et al.*, 2017).

The main disadvantages of mechanically collimated cameras in principle are the reduced detection efficiency (solid angle) due to the partial absorption of secondary radiation by the collimating device and their bulkiness. Electronically collimated cameras remove the need for physical collimation by using Compton kinematics to restrict the possible direction of travel of incident photons to a cone. For this reason this type of camera is also known as a Compton camera. Compton cameras typically consist of two detection stages: a scatterer and an absorber. The scatterer is made up of one or more thin (compared to the range of the scattered photons) detectors in which the photons undergo Compton scattering, whilst the absorber is made of thick detectors, often scintillators, aimed at completely absorbing the photons. Using accurate information about the position and deposited energy of coincident events in both stages allows one to deduce the initial energy of the photon (assuming that no energy has escaped the system) and thus the photon scattering angle (Schönfelder *et al.*, 1973). The emission point of the photon thus lies on the surface of a cone whose vertex is described by the position of the interaction in the scatterer and whose axis is described by the straight line between the interaction points in the scatterer and the absorber. Reconstruction of the emission point can be achieved via analytic or iterative algorithms. In particular, the analytic line-cone reconstruction uses the intersection of the Compton cone with the primary beam axis, if the spatial information of the primary ion beam is available.

Compton imaging for the online control of hadron therapy has been investigated via simulations and experimentally using prototype devices both under laboratory conditions (Golnik *et al.*, 2016; Kasper *et al.*, 2020; Koide *et al.*, 2018; McCleskey *et al.*, 2015; Muñoz *et al.*, 2017; Richard *et al.*, 2011; Rohling *et al.*, 2017; Ros García *et al.*, 2020; Solevi *et al.*, 2016; Taya *et al.*, 2016; Thirolf *et al.*, 2016) and in a more clinically-relevant environment (Draeger *et al.*, 2018; Hueso-González *et al.*, 2017; Kurosawa *et al.*, 2012). More recently, Fontana *et al.* (Fontana *et al.*, 2020) reported on the performance of a Compton camera prototype under construction by the French CLaRyS collaboration. The CLaRyS Compton camera consists of a silicon-semiconductor based scatterer and a scintillating absorber. The scatterer is comprised of seven plane silicon detectors and the absorber is comprised of an array of $Bi_{12}GeO_{20}$ scintillating crystals (Fontana *et al.*, 2020; Krimmer *et al.*, 2015). This camera is intended to be coupled to a beam hodoscope for beam-position and TOF measurement (Allegrini *et al.*, 2021). The precision of the camera for the calculation of the Bragg peak fall-off position was compared using two different reconstruction methods: an iterative maximum likelihood expectation maximisation (MLEM) reconstruction (Maxim *et al.*, 2015) and the analytic line-cone reconstruction (Roellinghoff *et al.*, 2011). Based on Monte Carlo simulations using 10^8 primary protons of 160 MeV in single proton counting mode incident on a PMMA phantom, a fall-off position precision of 2.6 mm (1σ) was reported for the MLEM reconstruction method, which is comparable to the precision (1σ) reported for the IBA KES camera (Fontana *et al.*, 2020). For clarity, all references to precision in this manuscript relate to the statistical precision. The main disadvantage of iterative techniques to reconstruct the γ emission position is the complexity of the algorithms, translating to a relatively long calculation time, which is a limiting factor for online range verification. The line-cone reconstruction is much simpler since the possible solutions from a coincidence pair are reduced from the surface of a cone to just two points at the intersection of that cone with the beam axis. The reconstruction of a γ emission profile for 10^8 incident protons can be performed on a time-scale of the order of seconds or less for analytic algorithms such as the line-cone reconstruction, compared to orders of magnitude longer for convergence of an iterative algorithm. Actual times depend of course on the complexity of the algorithm in question and the machine architecture, but even with modern GPU processing, it is difficult to envisage iterative reconstructions in a time-scale comparable to that of an analytic reconstruction. A lower precision, however, of about 8 mm under the same conditions using the line-cone reconstruction was reported by Fontana *et al.* (2020), with the authors attributing the degradation in precision to the additional noise due to the inclusion of the two line-cone reconstructed points in the γ-emission profile. Clearly one, or perhaps both in the case of partial energy absorption, of these events is false. One possible strategy to improve the reconstruction would consist in setting *a priori* filters excluding intersection points outside the expected region of interest (outside the patient and beyond the expected Bragg peak), and weighting the selected solutions accordingly or use them as a baseline to compare against. Alternatively, in the present paper, we intend to evaluate the potential of the time of flight (TOF), being the sum of projectile transient time and photon flight time to the absorber such as in prompt-γ timing (Golnik *et al.*, 2014; Marcatili *et al.*, 2020) information in order to reduce the possible two solutions of the line-cone reconstruction to just one.

The aim of the present study was to propose a method of solution rejection based on TOF using a Compton camera and the line-cone reconstruction method. Since in single-proton mode measurements of TOF are limited primarily by the temporal resolution of the absorber (Dauvergne *et al.*, 2020), the effect of absorber temporal resolution in the range 100 ps to 1.3 ns RMS on the precision of the measured fall-off position was investigated. The upper limit, 1.3 ns, was chosen from the measured temporal resolution of the BGO absorber of the CLaRyS Compton camera (Fontana *et al.*, 2020) and the lower limit, 100 ps, was chosen based on the limits of existing technology for monolithic, large volume scintillators (Lecoq *et al.*, 2020). The $CeBr_3$ absorber block of the Compton camera developed by Damavan Imaging (Rosières près Troyes, France) (Iltis *et al.*, 2018) for the localisation of radioactive sources is reported to have a temporal resolution of about 100 ps RMS at 511 keV. Moreover, coincidence time resolution of 100 ps was achieved in coincidence measurements with proton beams, using diamond detectors for projectile time stamp and monolithic scintillators for prompt γ (Marcatili *et al.*, 2020). The study was performed using GATE Monte Carlo simulations (Jan *et al.*, 2011; Sarrut *et al.*, 2014) of a proposed upgraded version of the CLaRyS Compton camera, where the BGO absorber has been replaced by $CeBr_3$ and the geometry slightly modified to increase the sensitivity of the camera.

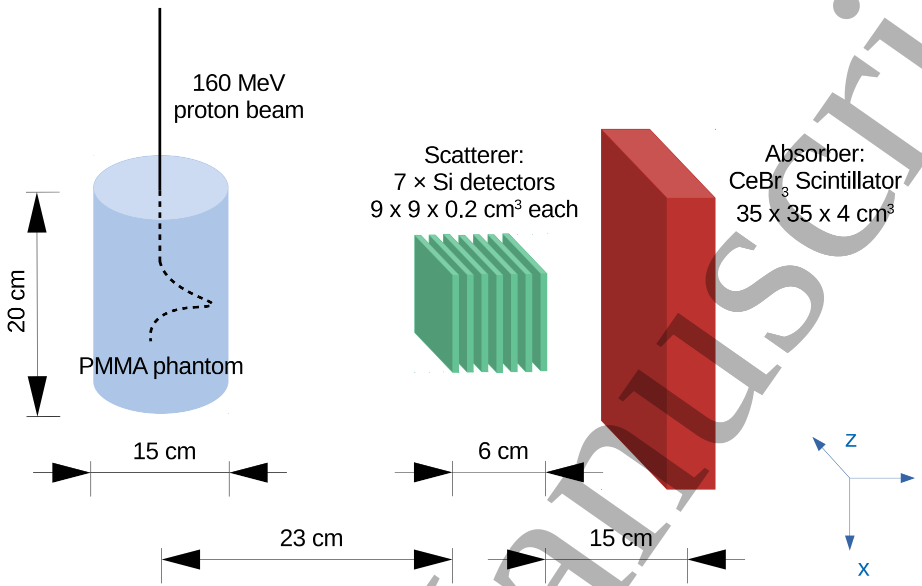

Figure 1: The geometry used in the GATE simulations. A Compton camera, comprised of 7 plane silicon detectors and a $CeBr_3$ scintillator, was positioned so as to detect prompt γ-rays generated in a polymethyl methacrylate (PMMA) phantom by an incident proton beam.

2. Methods

2.1. Detector

The CLaRyS Compton camera consists of a semiconductor based scatterer and a scintillating absorber. The scatterer is comprised of 7 plane silicon detectors with dimensions of $9 \times 9 \times 0.2$ cm^3 spaced 1 cm apart and the absorber is comprised of an array of 10×10 BGO scintillating crystals ($3.5 \times 3.5 \times 3$ cm^3 each) (Fontana *et al.*, 2020; Krimmer *et al.*, 2015). In order to realistically study the effect of the temporal resolution of the Compton camera on the precision of the fall-off position retrieval, the BGO absorber was replaced by a $35 \times 35 \times 4$ cm^3 block of $CeBr_3$. The energy resolutions of the scatterer and absorber detectors were modelled using an inverse square root law (Etxebeste *et al.*, 2020) based on the known resolutions of 1.1% FWHM at 1 MeV for Si (Fontana *et al.*, 2020) and 6.9% FWHM at 511 keV for $CeBr_3$ (Iltis *et al.*, 2018). The centre-to-centre distance between the last silicon plane detector and the $CeBr_3$ absorber was set to 15 cm. This geometry is illustrated in figure 1.

2.2. Simulation

The simulations were performed with GATE v8.0 using the QGSP_BIC_HP hadronic physics list (incorporating high precision neutron models) and the Livermore electromagnetic physics option in order to take into account low energy electromagnetic physics processes, atomic effects and Doppler broadening.

A Gaussian-shaped proton beam of $\sigma_x = \sigma_y = 2$ mm and energy 160 MeV (Gaussian spread of 2 MeV RMS) was generated with a rate sufficiently low to avoid fortuitous coincidences (Fontana *et al.*, 2020; Rohling *et al.*, 2017). As discussed by Dauvergne *et al.* (2020), such a rate corresponds to single proton counting mode, enabling non-ambiguous correlation between the primary ion and the detected prompt γ, at intensities reduced by a factor 100-1000 with respect to clinical ones, depending on the accelerator type. For simplicity in the simulation a current of 1 proton/µs, or 0.16 pA, was used. The beam was directed towards a cylindrical phantom of polymethyl methacrylate (PMMA), with dimensions 15 cm (diameter) × 20 cm (height), a mass density of 1.195 g/cm^3 and orientation along the beam axis. Information relevant to the particles crossing the entrance of the phantom was recorded in a phase space file, including their three-dimensional position and time of entrance. No uncertainty is associated with the time of entrance. In the following, the time resolution associated with the TOF will represent the resolution of both the beam hodoscope and the absorber. In practice, the beam hodoscope (not simulated here) is placed close to the phantom, such that the entrance time in the phantom is within picoseconds of the the hodoscope time stamp, independently of beam energy spread and angle. The uncertainties of both detectors add quadratically, and 100 ps RMS is the minimum value based on measurements performed using a diamond detector for protons and a fast monolithic scintillator for PG (Marcatili *et al.*, 2020). Therefore, it was not necessary to consider the uncertainty of the time of entrance and the time of photon absorption separately. For simplicity and better understanding of the following results, we discuss the TOF resolution as if it were entirely due to the absorber. The position of primary protons at the phantom entrance was later used to describe the trajectory of the protons for the line cone reconstruction, and the time used as a reference for the TOF. Experimentally, this would correspond to a beam-tagging hodoscope which is under development by the CLaRyS collaboration, using either scintillating fibres (Krimmer *et al.*, 2015) or diamond detectors (Gallin-Martel *et al.*, 2018) to ensure a high temporal resolution of the order of 100 ps RMS (Marcatili *et al.*, 2020).

The Compton camera was positioned such that the first scatterer plane was at a distance of 23 cm from the phantom axis, with the detector parallel to the beam axis. Simulations were performed at two different positions: centred on the centre of the PMMA phantom, i.e., 100 mm downstream of the phantom entrance, and centred approximately at the expected Bragg peak position. From the NIST PSTAR database (Berger, 2002), the projected range of 160 MeV protons in PMMA is 151.5 mm, which was approximated to 150 mm downstream of the phantom entrance. The aim of change

Table 1: The resolutions assigned to the scatterer and absorber in the simulations. Values for the scatterer were obtained from Fontana *et al.* (Fontana *et al.*, 2020) and values for the $CeBr_3$ absorber were taken from the measurements by Iltis *et al.* (Iltis *et al.*, 2018). The spatial resolution of the detectors is assumed to be constant, whereas their energy resolutions are inversely proportional to $\sqrt{E}$, where E is the photon energy.

Resolution (σ)	Scatterer	Absorber
spatial (mm)	2	2
energy	1.1% at 1 MeV	7% at 511 keV
temporal (ns)	15	variable (0–1.3)

in position was to investigate the effect of the decreased detection efficiency of the camera off-axis as a result of the limited field of view. Interactions of particles with the Compton camera were digitised using the Gate Compton camera imaging module, *CCMod* (Etxebeste *et al.*, 2020). The three dimensional position, time and energy deposition of each interaction were stored, and lists of coincidences within a 40 ns window were created. Coincidences involving multiple interactions in the scatterer were ignored, whilst for multiple interactions in the absorber, the energy deposition of each interaction was summed and the weighted average position of the interactions was found.

The spatial and energy resolutions were modelled within GATE using the spatial blurring and local energy blurring modules respectively. These modules apply a Gaussian blurring to the recorded energy and spatial data. The temporal resolution was modelled using a Gaussian random number generator during the post-processing stage. The values of the energy, spatial and temporal resolutions assigned to each part of the camera are given in Table 1.

It is important to note that the present simulations do not account for fortuitous coincidences and that only prompt γ-rays are considered. Scattering of prompt γ-rays inside the phantom as well as incomplete absorption in the $CeBr_3$ absorber have however been taken into account.

2.3. Line-cone reconstruction

Energy filters were applied during the construction of Compton cones for the recorded coincidence events. Minimum thresholds of 50 keV and 100 keV were applied for the energy deposited in a single scatterer layer and the corresponding energy deposited in the absorber respectively. An additional minimum threshold of 1 MeV for the total energy deposition (sum of energies deposited in the scatterer and the absorber) was applied in order to reduce reconstructions resulting from partially absorbed photons. Additionally, photons with energies less than 1 MeV are less correlated to the proton range since they have a high probability of being scattered in the PMMA phantom, or may be delayed γ-rays resulting from β^+ annihilation at 511 keV.

For each coincidence pair satisfying the conditions on the energy deposition, a

Compton cone was constructed. The apex of the cone was described by the interaction position in the scatterer, the axis of the cone was described by the straight line joining the interaction points in the absorber and the scatterer, and the opening angle of the cone was described by Compton kinematics:

$$\cos\theta = 1 - m_e c^2 \left(\frac{1}{E_1} - \frac{1}{E_0}\right) \tag{1}$$

where θ, the Compton scattering angle, describes the half-opening angle of the cone, $m_e c^2 = 0.511$ MeV, E_0 is the initial energy of the photon and E_1 is the energy of the scattered photon. The surface of the Compton cone describes the possible emission points of the photon if the following conditions are assumed to be true:

- that the energy absorbed by the absorber, ΔE_2, is equal to the energy of the scattered photon, E_1,
- that the sum of the energies absorbed by the scatterer and the absorber, $\Delta E_1 + \Delta E_2$ is equal to the energy of the photon, E_0.

The line-cone reconstruction takes advantage of the additional information about the proton beam provided by the beam-tagging hodoscope, or in this case by the phase space file generated at the entrance of the PMMA phantom, to minimise the number of possible solutions for each coincidence pair to just the two points of intersection of a line and the Compton cone. The line is described by the trajectory of the correlated proton, i.e., the primary proton that interacted in the PMMA phantom giving rise to the emission of a particular photon detected by the Compton camera. To find the correlated proton for each coincidence pair, a window of 8 ns was applied to the total TOF, i.e., the difference in time between the interaction in the absorber and the time of entrance of the proton in the PMMA phantom. This window was chosen from simulated TOF distributions of γ-rays and neutrons generated by interactions of primary protons with the phantom.

To select the most probable solution of the two solutions provided by the line cone reconstruction, the temporal information provided by the camera was used. For each of the two solutions, a TOF was estimated based on the TOF of the correlated proton, TOF_p, in the PMMA phantom, and the TOF of a γ, TOF_γ with a trajectory described by the reconstructed emission point and the positions of interaction in the scatterer and the absorber, similarly to prompt-γ timing (Golnik *et al.*, 2014). In practice, the TOF_p is unknown, so a model of the TOF_p as a function of γ emission points was created based on simulated interactions of 1×10^7 primary protons of 160 MeV incident on the PMMA phantom. To create the model of TOF_p, emitted γ-rays with energies above 1 MeV which had not undergone any scattering in the phantom were traced back to the beginning of their track, i.e., their emission point. The time elapsed between the entrance of the proton in the phantom, the reference time t_0, and the emission of the γ-ray, t_γ, was plotted as a function of the γ emission depth x and a polynomial function f was fitted using least-squares minimisation. The elapsed time between the estimated

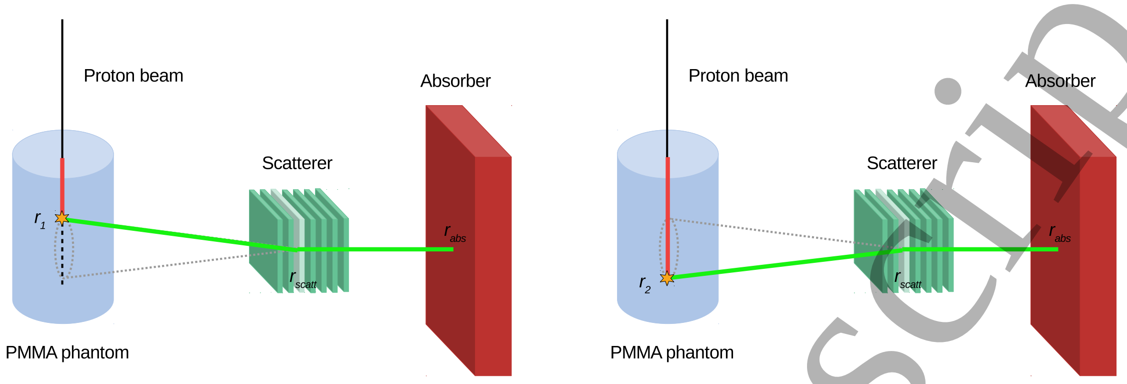

(a) Solution r_1 (b) Solution r_2

Figure 2: (a) The proton and γ tracks corresponding to the solution $r_1 = (x_1, y_1, z_1)$ with TOF_{est_1} and (b), the proton and γ tracks corresponding to the solution $r_2 = (x_2, y_2, z_2)$ with TOF_{est_2}. In both cases, the star represents the solution, or the reconstructed emission point of the γ-ray, the red line represents the track of the proton and the green line represents the track of the γ-ray.

γ emission and the reference time, $t_\gamma - t_0$ is assumed to be equal to the TOF_p. For each solution of the line-cone reconstruction, the TOF_p was found by applying the fitted polynomial function f to the reconstructed emission point, as described by equation 2.

$$TOF_{p,i} = f(x_i) \tag{2}$$

where i is an integer of value 1 or 2, identifying each line-cone solution, and x_i is the coordinate of the emission point on the proton beam axis for solution i.

The distance travelled by the γ-ray was then calculated using the reconstructed emission point $\boldsymbol{r}_i = (x_i, y_i, z_i)$ and the interaction positions in the scatterer and the absorber, $\boldsymbol{r}_{scatt} = (x_{scatt}, y_{scatt}, z_{scatt})$ and $\boldsymbol{r}_{abs} = (x_{abs}, y_{abs}, z_{abs})$ respectively. The TOF_γ was then found using equation 3:

$$TOF_{\gamma_i} = \frac{1}{c}\left(\|\boldsymbol{r}_{scatt} - \boldsymbol{r}_i\| + \|\boldsymbol{r}_{abs} - \boldsymbol{r}_{scatt}\|\right) \tag{3}$$

The estimated TOF for each solution, TOF_{est_i}, is then found by the sum of TOF_{p_i} and TOF_{γ_i}:

$$TOF_{est,i} = TOF_{p,i} + TOF_{\gamma,i} \tag{4}$$

The total tracks corresponding to $TOF_{est,1}$ and $TOF_{est,2}$ are illustrated in Figure 2.

The estimated TOF for each solution was subsequently compared to the TOF provided by the Compton camera, TOF_{CC}, which is defined as the difference between the time of the interaction in the absorber, t_{abs} and the reference time, or the time that the corresponding proton crossed the entrance of the phantom, t_0. The TOF_{CC} is given by equation 5:

$$TOF_{CC} = t_{abs} - t_0 \tag{5}$$

The comparison of the estimated TOF for each solution, TOF_{est_i} to the TOF_{CC} is made by finding the absolute value of their difference, which will be referred to as ΔTOF_i and is calculated using equation 6.

$$\Delta TOF_i = \mid TOF_{CC} - TOF_{est,i} \mid \qquad (6)$$

Several criteria can be used to make a selection of the most probable line-cone solution based on ΔTOF_i. The simplest method is selection of the solution having the smallest ΔTOF, that is, the solution with a TOF_{est} which is closest to the TOF_{CC}. This method will only reject one of the two solutions, however there may be cases where the two line-cone solutions are very different from the real γ emission point. This may occur, for example, when the interaction in the absorber used to describe the apex of the cone in the line-cone reconstruction is not one in which the total energy of the γ-ray is absorbed, or for γ-rays which undergo scattering within the phantom prior to interacting with the Compton camera. For these cases, a method which can reject both of the solutions for given conditions is required. In this study, an upper threshold of 2σ, where σ is the root mean squared temporal resolution of the camera, was placed on the ΔTOF. The solution which is selected is thus the solution with the minimum ΔTOF which satisfies the condition $\Delta TOF \leq 2\sigma$. If neither solution satisfies this latter condition, then both solutions are disregarded.

2.4. Calculation of the fall-off position and its precision as a function of temporal resolution

The γ-ray spatial fall-off positions were calculated using the procedure outlined in (Fontana *et al.*, 2020; Huisman, 2017; Roellinghoff *et al.*, 2014) using a reference profile for each value of temporal resolution investigated. The reference profiles are defined as the reconstructed γ emission profiles at high statistics: 2×10^{10} incident protons. They were first smoothed using a one-dimensional cubic spline function, then a model of each reference function was obtained by interpolating the smoothed data over the range $x = -200$ mm to 200 mm relative to the centre of the phantom ($x = 0$), in steps of 0.5 mm. A baseline, equal to the lowest 25% of data was set and the distal maximum found. The fall-off position was then defined as the position for which the height of the histogram is equal to half the difference between the distal amplitude and the baseline.

The precision was measured using the method described by Fontana *et al.* (2020), which is based on the difference between the fall-off position (FOP) predicted by a reference γ emission profile (according to the treatment planning for example) and the detected one. Firstly, 100 lower-statistic profiles based on 1×10^8 primary protons each, selected at random from the total of 2×10^{10} protons such that no event was selected more than once, were created. Then for each value of temporal resolution, the model of the reference profile was fitted to each of the lower statistics profiles by shifting the reference profile in the range -30 mm to 30 mm relative to its initial position, in steps of 1 mm, after area normalisation. For each step the reference profile was compared to the lower statistics profile bin-by-bin by calculating χ^2 as in equation 7:

$$\chi^2 = \sum_{i=1}^{N} (y_{sample,i} - y_{ref,i})^2 \tag{7}$$

where i is the bin number, N is the total number of bins, $y_{sample,i}$ is the number of events in bin i of the lower statistics profile and $y_{ref,i}$ is the number of counts (scaled to the amplitude of the sample profile) in bin i of the reference profile. The global minimum, χ^2_{min}, was found for each profile and the process was repeated for the 100 lower statistics profiles. The precision of the fall-off position for each value of temporal resolution was defined as the standard deviation of the distribution of fall-off positions obtained for the 100 lower statistics profiles.

3. Results

3.1. Line-cone reconstruction

The time of flight of protons, TOF_p, used to estimate a time of flight for each of the two line-cone solutions was based on a model derived from simulated interactions of protons incident on the PMMA phantom.

A mathematical model of the TOF_p as a function of γ-emission points was found from a least-squares minimisation fit of a 4th order polynomial function to the histogram in figure 3(a).

Spatial distributions of the proton time of flight (assumed to be equal to the time elapsed between a proton traversing the hodoscope and the emission of a prompt γ-ray, $t_\gamma - t_0$) as a function of the γ emission points (both real and reconstructed for different values of temporal resolution from 0 to 1000 ps) are shown in figure 3. Here, the γ-emission point is the beam-axis coordinate of the two solutions (no solution selection has been made) and the $t_\gamma - t_0$ for each of the two solutions is the subtraction of the calculated γ TOF from the total TOF.

The comparison of line-cone reconstructed γ-emission profiles for each temporal resolution (and thus selection criterion) and each Compton camera position is illustrated in Figure 4. The profiles have each been normalised to their respective maximum values and compared with the real emission profile of γ-rays with energies above 1 MeV obtained from the phase space file. When decreasing the temporal resolution and applying the selection criteria to disregard either one or both of the reconstructed points, the relative contribution of points reconstructed outside the phantom is observed to decrease. The observed fall-off at the distal-end of the Bragg peak also becomes sharper.

The number of contributing gammas normalised to the number of impinging protons (profile integrals) as a function of temporal resolution is plotted in figure 5, with and without solution discrimination and for both camera positions. Very little to no difference is observed between the two camera positions. When no solution discrimination is performed, the area under the profile is almost constant, with a slight

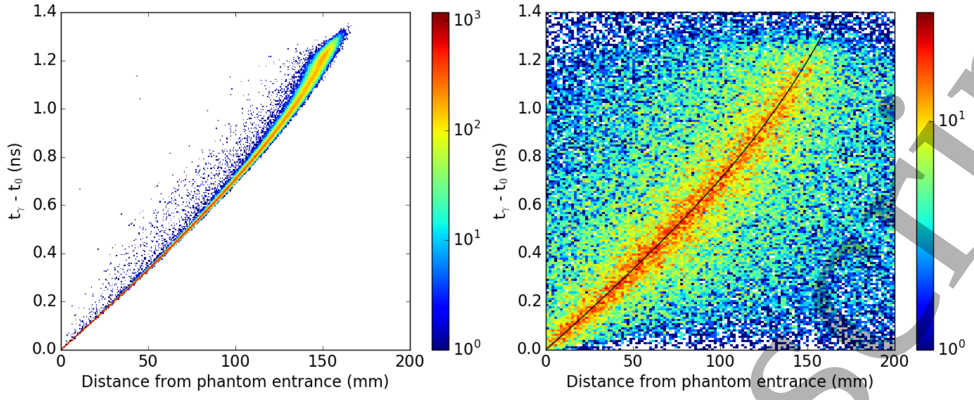

(a) Real emission point

(b) 0 ps

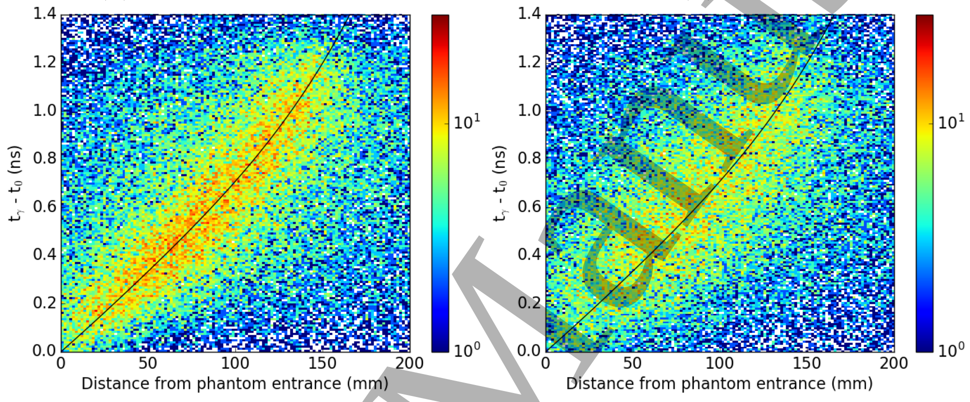

(c) 100 ps

(d) 200 ps

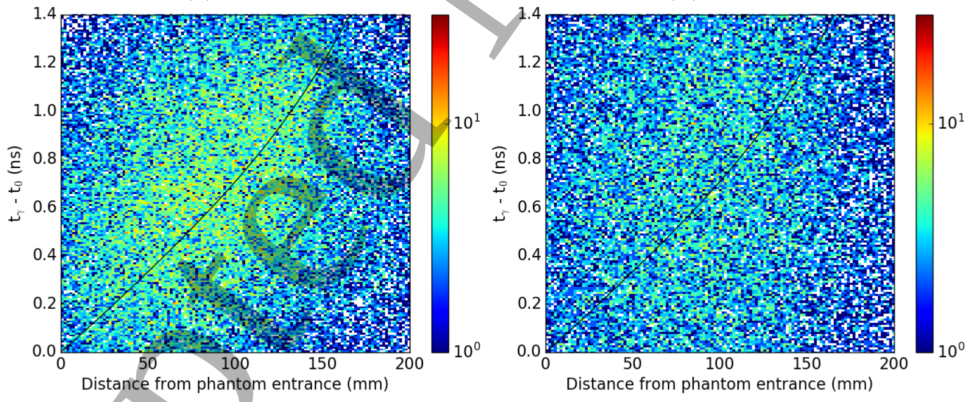

(e) 500 ps

(f) 1000 ps

Figure 3: 2D histograms representing the proton time of flight, TOF_p, as a function of the emission point of the correlated γ photon. Figure (a) is based on the real photon emission point recorded in the phase space file and figures (b) to (f) are based on the reconstructed emission points for temporal resolutions of 0, 100, 200, 500 and 1000 ps respectively. The emission points are the beam-axis coordinates of the two solutions (no selection has been made). The solid black curve is the 4th order polynomial fit to (a).

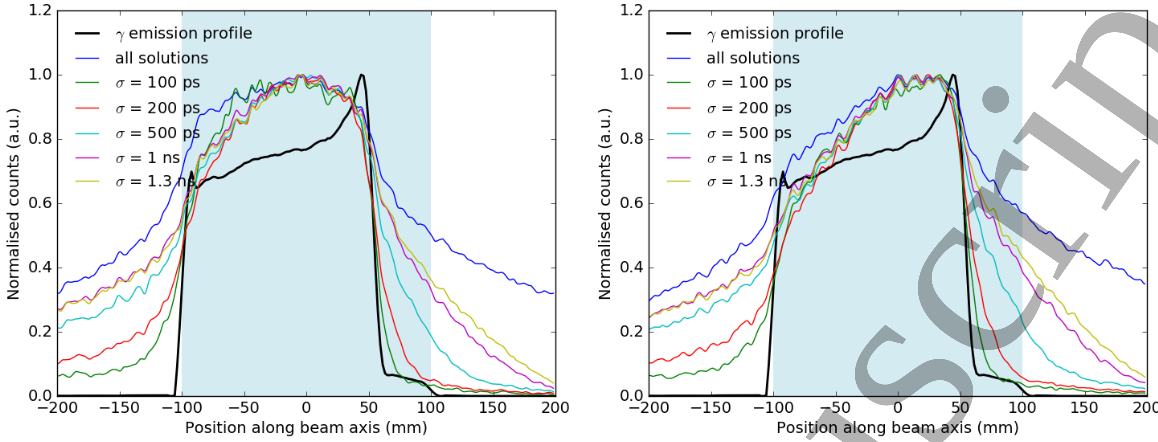

(a) $x = 0$ mm (b) $x = 50$ mm

Figure 4: Line-cone reconstructed γ-emission profiles for a 160 MeV proton beam (10^7 incident protons for the γ emission profiles in black, $2{\times}10^{10}$ for all others) in single proton counting mode with (a) the Compton camera centred on the centre ($x = 0$ mm) of the PMMA phantom and (b) the Compton camera centred close to the expected Bragg peak position ($x = 50$ mm). The shaded region represents the length of the PMMA phantom in the direction of beam travel. Each curve has been normalised to its maximum value.

decrease observed for temporal resolutions of 1 and 1.3 ns due to the decreased number of events occuring within the 40 ns coincidence window. The observed decrease in area with improving temporal resolution is a result of improved selection of full-absorption events: with insufficient temporal resolution, the discrimination method is unable to determine when both solutions are incorrect, for example due to partial energy absorption in the absorber.

3.2. Calculation of the fall-off position and its precision as a function of temporal resolution

The fall-off position, defined as the point where the height of the prompt γ emission profile is half of the difference between the distal amplitude and the baseline, was calculated for each of the high statistic reference profiles. An example of the reference profiles for a temporal resolution of 0.1 ns is given in figure 6. With the Compton camera centred on the centre of the PMMA phantom, the fall-off position was found to occur at 55.3 mm (155.3 mm from phantom entrance), compared to 55.9 mm (155.9 mm from phantom entrance) when the camera was centred on the expected Bragg peak position. The fall-off position calculated for the profile of known γ emission points recorded by the simulation was 54.4 mm (154.4 mm from the phantom entrance). For comparison, the PSTAR (Berger, 2002) prediction of the projected range of 160 MeV protons in PMMA of the same density used in the simulations is 151.5 mm, whereas the R_{50} and R_{80} values calculated for the simulated depth-dose of 160 MeV protons in PMMA were

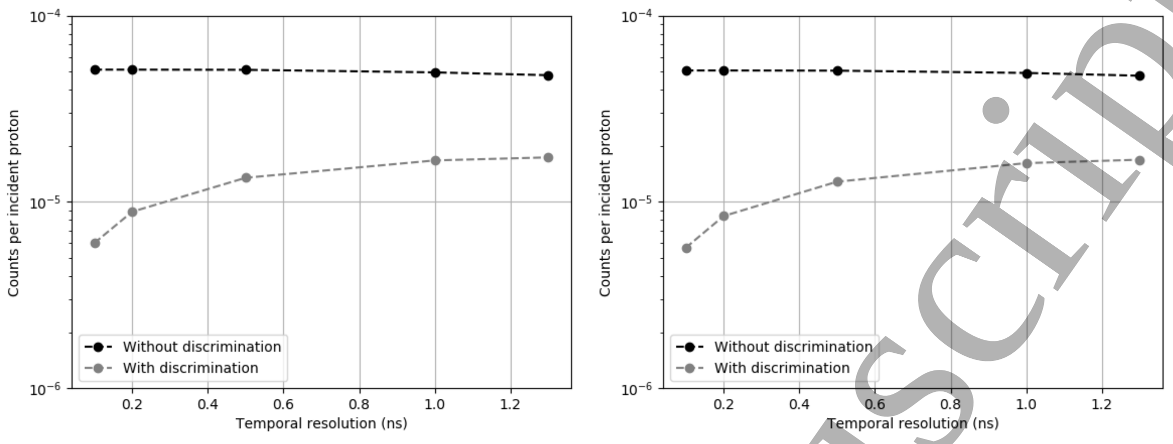

(a) On the center of the phantom (b) On the expected Bragg peak position

Figure 5: Area under the profiles displayed in figure 4 without normalisation as a function of temporal resolution with (a) the Compton camera centred on the centre of the PMMA phantom and (b) the Compton camera centred close to the expected Bragg peak position. The corresponding profiles were obtained for a 160 MeV proton beam ($2{\times}10^{10}$ incident protons) in single proton counting mode.

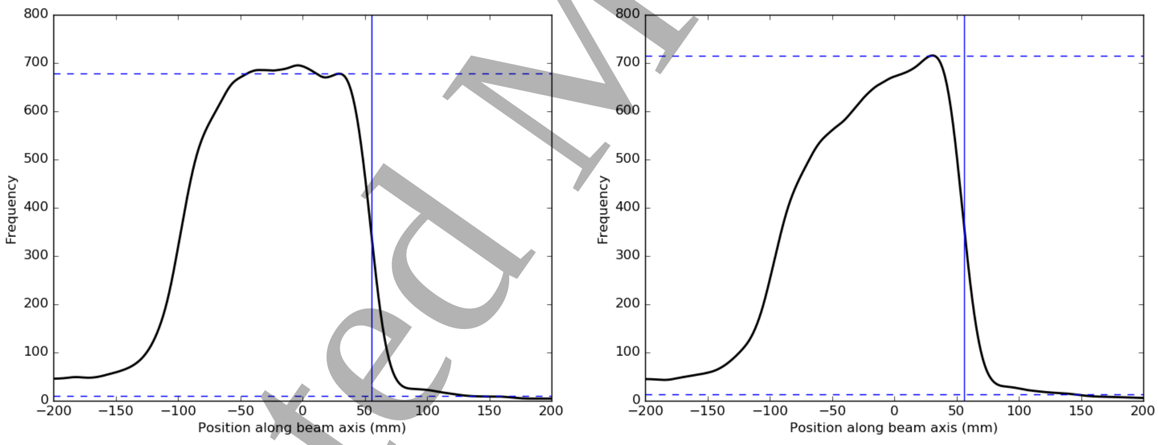

(a) On the centre of the phantom (b) On the expected Bragg peak position

Figure 6: An example of a reference profile for σ = 100 ps (timing resolution) for a 160 MeV proton beam ($2{\times}10^{10}$ incident protons) with the camera centred on (a) the centre of the phantom and (b) on the expected Bragg peak position. The profiles have been smoothed using a cubic spline function. The markup illustrates the method used to calculate the fall-off position. The two horizontal dashed lines illustrate the distal amplitude and the baseline and the solid vertical line illustrates the fall-off position, calculated as the position where the height of the histogram is equal to half the difference between the distal amplitude and the baseline.

155.5 mm and 153.5 mm respectively.

As mentioned in Methods, for each value of temporal resolution the relevant

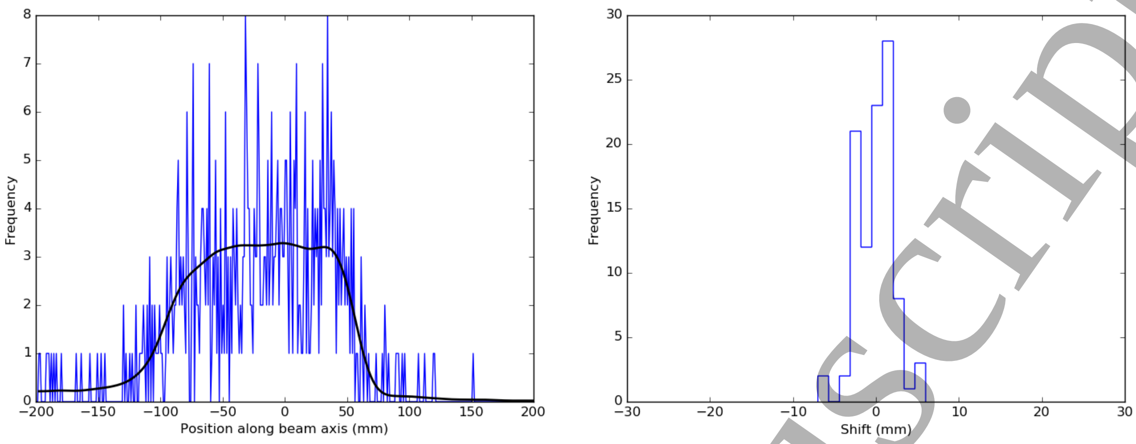

(a) Example of recorded shift (b) Shift distribution

Figure 7: To calculate the precision of the calculated fall-off position, the high statistics curve was scaled and fitted to each of the 100 lower statistics data subsets. An example for $\sigma = 100$ ps is shown in (a) where the scaled reference curve (2×10^{10} incident protons of 160 MeV) is in black and bold, and the lower statistics subset (10^8 incident protons of 160 MeV) is in blue. The high statistics curve was shifted between -30 mm and $+30$ mm relative to its initial position and the minimum χ^2 found. The required shift for each data subset was recorded. An example of shift distribution is shown in (b). The precision is defined as the standard deviation of the 100 recorded values of required shift.

reference profile was scaled and fit to 100 low statistics γ emission profiles. The fit was obtained by shifting the reference profile laterally and finding the shift corresponding to the minimum χ^2 value. The precision of the calculated fall-off position is then said to be the standard deviation of the shift values recorded for the 100 profiles. This process is illustrated in figure 7.

The precision of the fall-off position as a function of temporal resolution for each of the camera positions studied is plotted in figure 8. As expected, for both camera positions the precision remains approximately constant as a function of temporal resolution when no solution discrimination is performed (i.e., both solutions are kept in the profile). Also non-surprisingly, the precision of the fall-off position improves with improving temporal resolution, decreasing from 4–4.5 mm at 1.3 ns RMS temporal resolution to 2.2–2.4 mm at 100 ps RMS temporal resolution. Whether the Compton camera is centred at the centre of the phantom or at the expected Bragg peak position appears to make little to no difference on the precision of the measured fall-off position. A small difference, however, was noted for the systematic uncertainty, or mean absolute shift, for the two camera positions. When the camera was centred on the expected Bragg peak position, the mean shifts were -0.08 mm (with discrimination) and 0.18 mm (no discrimination), compared to 0.16 mm and 0.58 mm respectively when the camera was centred on the centre of the phantom. No relationship between the temporal resolution

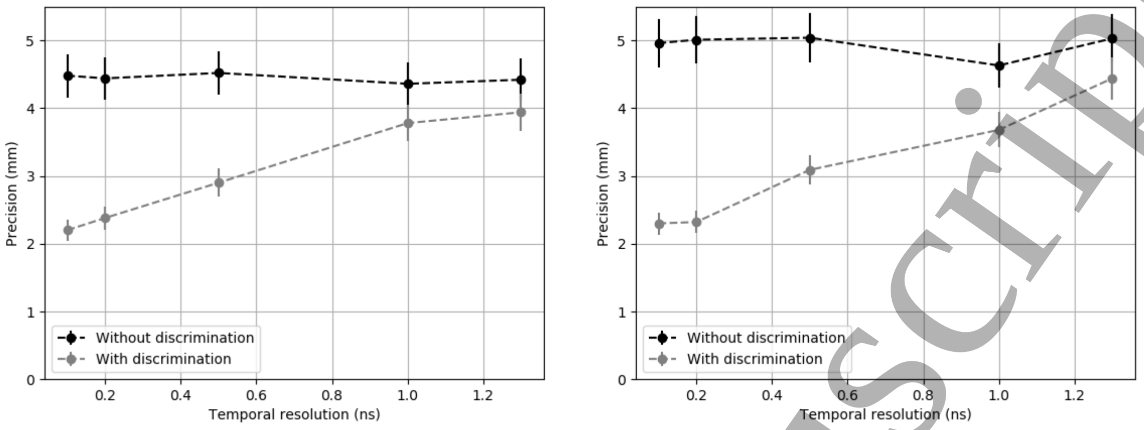

(a) On the centre of the phantom (b) On the expected Bragg peak position

Figure 8: Precision (1σ) of the calculated Bragg peak fall-off position as a function of temporal resolution for a 160 MeV proton beam (10^8 incident protons) with (a) the Compton camera centred on the centre of the PMMA phantom and (b) the Compton camera centred on the expected Bragg peak position. For each camera position, a comparison is made between the precision measured with and without solution discrimination.

and the determined shift value was found.

4. Discussion

A method of line-cone solution discrimination based on time of flight (proton + γ-ray) has been proposed and implemented to investigate. The method is used to investigate via Monte Carlo simulation the influence of the temporal resolution on the precision of the prompt γ fall-off precision in Compton camera imaging. The proposed discrimination method involves a comparison of the TOF recorded by the camera to estimated TOFs for each of the two possible γ emission points produced by the line-cone reconstruction. The estimated TOFs are the sum of the γ TOF, easily calculated from its path length and velocity, c, and the proton TOF which is estimated from a polynomial fit to the distribution of γ emission times as a function of depth in the phantom obtained from the simulation. This method requires a beam tagging hodoscope to be placed at the beam exit window and is intended for use in single proton counting mode, but could also be operated with ultra short bunches, since the timing resolution includes the bunch time length.

Upon observation of figure 3, four potential limitations of the polynomial fit might seem apparent: (1) the model relies on *a priori* information of proton interactions in the phantom obtained via simulation, (2) the model does not take into account the lateral straggling of the protons observed towards the Bragg peak (~150 mm), (3) the model is extrapolated beyond the ion range where it no longer makes any physical sense, and (4) a homogeneous target is considered. However, when comparing the model to the same distributions of data obtained only from reconstructed γ emission positions and TOF, i.e., information which can be experimentally obtained (figures 3(b)–3(f)), it is observed to well describe the centre of mass of the distribution, in which the lateral straggling is not visually apparent. Additionally, if the model were to end at the end of the ion range a bias would be introduced when discriminating solutions: all solutions occuring beyond the model would naturally be rejected and shifts in the fall-off position compared to the treatment plan resulting from potential patient mispositioning, changes in morphology etc. may go undetected. It is also worth noting that the model obtained via simulations using a homogeneous, cylindrical PMMA phantom for the purposes of this study would likely not be appropriate for line-cone solution discrimination in a clinical setting. It could be envisaged however to obtain the relevant model via simulation using patient CT data. CT-based simulations will also be used to generate the profiles and the corresponding timing distributions.

The influence of the camera position relative to the phantom is observed not to have a strong influence on the shape of the reconstructed γ emission profile (figure 4). When the camera is centred on the expected Bragg peak position, about 150 mm from the phantom entrance, the relative number of photons rises more slowly towards the maximum, which is close to the Bragg peak. When the camera is centred on the centre of the phantom, the profile is closer to symmetric, with its maximum at the centre. The fall-off at the distal end of the Bragg peak appears similar, and from figure 8, no difference (within uncertainty) in the precision of the fall-off position is observed. Finally, as observed in figure 5, the sensitivity of the camera is approximately the same for the different positions considered despite the difference in the shape of the reconstructed profiles.

The influence of temporal resolution on the precision of the fall-off position is also displayed in figure 4. The relative number of reconstructed events outside the phantom decreases with improving temporal resolution, and the distal fall-off of the reconstructed profile is observed to become steeper, approaching that of the real γ emission profile obtained from the simulation. As a result, the precision of the fall-off precision also improves with improving temporal resolution, achieving a value of 2.3 ± 0.15 mm at 200 ps resolution regardless of the camera position (between 100 and 150 mm relative to the phantom entrance). Improving the temporal resolution from 200 to 100 ps has little to no effect on the precision. This value is a pronounced improvement of the 4.5–5 mm precision observed when no solution discrimination is performed, and is comparable with the precision determined via simulations by Fontana *et al.* (Fontana *et al.*, 2020) for the CLaRyS Compton camera using an MLEM reconstruction for the same number of incident protons. At 1.3 ns temporal resolution, the precision is 4–4.5 mm which is only a very small improvement compared to the case where no solution discrimination is performed. There is therefore not much to be gained by applying the solution discrimination technique to the current CLaRyS Compton camera with a BGO absorber. For the latter, spatial filtering strategies are required, excluding, for instance, reconstructed events outside the target, or even outside the expected proton range, as mentioned in the introduction. In the present study, such filters were not found to significantly improve the contrast of the reconstructed profile (please refer to the supplementary material). Moreover, the *a priori* knowledge of the phantom position and beam range may induce a bias.

The improved precision with improving spatial resolution however comes at the expense of reduced profile statistics, or an effective reduction in detection efficiency. In figure 5 the absolute number of counts corresponding to the profiles displayed in figure 4 are observed to decrease with improving temporal resolution, by a factor of approximately 3 for example between temporal resolutions of 1.3 and 0.1 ns. This is due to the fact that as the tolerance on the difference between measured and estimated TOF becomes smaller with improving temporal resolution, the number of cases where both of the line-cone solutions are rejected increases. If both of the line-cone solutions are rejected it is because they are both assumed to be incorrect according to the selection criteria. Incorrect line-cone solutions may have the following causes:

(i) false coincidences,
(ii) events from particles or photons other than prompt γ-rays,
(iii) scattering of the γ-rays within the phantom
(iv) incomplete absorption in the absorber

In this work, steps were taken to reduce both (ii) and (iii) by using minimum energy thresholds on events recorded by the scatter and absorber (50 and 100 keV respectively), plus an additional threshold on the sum of the two (1 MeV). Incomplete absorption is assumed to be the main cause of incorrect line-cone solutions. The rate of decrease in the area increases quickly below 500 ps. Unlike for integral detection systems where ultra-fast timing at the level of 100 ps coincidence time resolution is a key for TOF-based imaging (Dauvergne *et al.*, 2020), here a temporal resolution of 100 ps provides little to no improvement in the precision compared to a temporal resolution of 200 ps, indicating that in this range of values of temporal resolution, the benefits of improved solution discrimination start to be outweighed by the degradation in precision caused by a reduced effective detection efficiency. For this reason, 200 ps should be recommended as the best compromise between sensitivity and precision of the fall-off position for the Compton camera described in this work. Increasing the detection efficiency of the camera, via optimisation of the geometry or otherwise, would intuitively lead to further improvements in the precision at values of temporal resolution of 100 ps and less. Work on both increasing the detection efficiency and pushing the limits of temporal resolution to improve the precision fall-off position measured in real-time using a Compton camera is ongoing within the CLaRyS collaboration and expected to be reported on in future communications.

5. Conclusion

A TOF-based method of discriminating the most likely reconstructed γ emission point from the pair of solutions yielded by the line-cone reconstruction for a Compton camera-detected coincidence has been proposed. This method was subsequently implemented in a Monte Carlo study of the effect of the temporal resolution of the Compton camera on the precision of the fall-off position in online ion-range verification. The temporal resolution was varied between 100 ps and 1.3 ns RMS. A precision of 2.30 ± 0.15 mm was achieved for 10^8 primary protons and a temporal resolution of 200 ps, corresponding with the current state-of-the-art. No further improvement was observed for a temporal resolution of 100 ps due to the reduced effective detection efficiency through the removal of double false reconstructed events arising mostly from incomplete energy deposition in the absorber. Further improvements to the fall-off position precision are expected to result from ongoing developments aimed at improving the detection efficiency and temporal resolution.

6. Acknowledgements

The authors acknowledge funding from ITMO-Cancer (CLaRyS-UFT project). This work was carried out within the framework of LabEx PRIMES (ANR-11-LABX-0063) and the EU Horizon 2020 project RIA-ENSAR2 (654 002). This work was partly supported by SIRIC LYriCAN: INCa-DGOS-INSERM-12563.

7. References

Allegrini, O., Cachemiche, J. P., Caplan, C. P. C., Carlus, B., Chen, X., Curtoni, S., Dauvergne, D., Negra, R. D., Gallin-Martel, M.-L., Herault, J., Létang, J. M., Morel, C., Testa, É., & Zoccarato, Y. (2021). *Characterization of a beam-tagging hodoscope for hadrontherapy monitoring* [arXiv:2101.02079].

Berger, M. (2002). *PSTAR: Stopping-power and range tables for protons* [https://physics.nist.gov/PhysRefData/Star/Text/PSTAR.html].

Dauvergne, D., Allegrini, O., Caplan, C., Chen, X., Curtoni, S., Etxebeste, A., Gallin-Martel, M.-L., Jacquet, M., Létang, J. M., Livingstone, J., Marcatili, S., Morel, C., Testa, É., & Zoccarato, Y. (2020). On the role of single particle irradiation and fast timing for efficient online-control in particle therapy. *Front. Phys.*, **8**, 567215.

Draeger, E., Mackin, D., Peterson, S., Chen, H., Avery, S., Beddar, S., & Polf, J. C. (2018). 3D prompt gamma imaging for proton beam range verification. *Phys. Med. Biol.*, **63**(3), 035019.

Etxebeste, A., Dauvergne, D., Fontana, M., Létang, J. M., Llosá, G., Munoz, E., Oliver, J. F., Testa, É., & Sarrut, D. (2020). CCMod: a GATE module for Compton camera imaging simulation. *Phys. Med. Biol.*, **65**(5), 055004.

Fontana, M., Ley, J.-L., Dauvergne, D., Freud, N., Krimmer, J., Létang, J. M., Maxim, V., Richard, M.-H., Rinaldi, I., & Testa, É. (2020). Monitoring ion beam therapy with a Compton camera: Simulation studies of the clinical feasibility. *IEEE Trans. Radiat. Plasma. Med. Sci.*, **4**(2), 218–232.

Gallin-Martel, M.-L., Abbassi, L., Bes, A., Bosson, G., Collot, J., Crozes, T., Curtoni, S., Dauvergne, D., De Nolf, W., Fontana, M., Gallin-Martel, L., Hostachy, J.-Y., Krimmer, J., Lacoste, A., Marcatili, S., Morse, J., Motte, J.-F., Muraz, J.-F., Rarbi, F. E., … Yamouni, M. (2018). A large area diamond-based beam tagging hodoscope for ion therapy monitoring. *EPJ Web Conf.*, **170**, 09005.

Golnik, C., Bemmerer, D., Enghardt, W., Fiedler, F., Hueso-González, F., Pausch, G., Römer, K., Rohling, H., Schöne, S., & Wagner, L. (2016). Tests of a Compton imaging prototype in a monoenergetic 4.44 MeV photon field – a benchmark setup for prompt gamma-ray imaging devices. *J. Inst.*, **11**, P06009.

Golnik, C., Hueso-González, F., Müller, A., Dendooven, P., Enghardt, W., Fiedler, F., Kormoll, T., Roemer, K., Petzold, J., Wagner, A., & Pausch, G. (2014). Range assessment in particle therapy based on prompt γ-ray timing measurements. *Phys. Med. Biol.*, **59**, 5399–5422.

Hueso-González, F., Pausch, G., Petzold, J., Römer, K. E., & Enghardt, W. (2017). Prompt gamma rays detected with a BGO block Compton camera reveal range deviations of therapeutic proton beams. *IEEE Trans. Radiat. Plasma. Med. Sci.*, **1**(1), 76–86.

Huisman, B. (2017). *Accelerated clinical prompt gamma simulations for proton therapy* (Doctoral dissertation). Université de Lyon.

Iltis, A., Snoussi, H., Rodrigues de Magalhaes, L., Hmissi, M. Z., Tata Zafiarifety, C., Zeufack Tadonkeng, G., & Morel, C. (2018). Temporal imaging CeBr$_3$ Compton camera: A new concept for nuclear decommissioning and nuclear waste management. *EPJ Web Conf.*, **170**, 06003.

Jan, S., Benoit, D., Becheva, E., Carlier, T., Cassol, F., Descourt, P., Frisson, T., Grevillot, L., Guigues, L., Maigne, L., Morel, C., Perrot, Y., Rehfield, N., Sarrut, D., Schaart, D. R., Stute, S., Pietrzyk, U., Visvikis, D., Zahra, N., & Buvat, I. (2011). GATE V6: a major enhancement of the GATE simulation platform enabling modelling of CT and radiotherapy. *Phys. Med. Biol.*, **56**, 881–901.

Kasper, J., Rusiecka, K., Hetzel, R., Kazemi Kozana, M., Lalik, R., Magiera, A., Stahl, A., & Wrońska, A. (2020). The SiFi-CC project – Feasibility study of a scintillation-fiber-based Compton camera for proton therapy monitoring. *Phys. Med.*, **76**, 317–325.

Knopf, A.-C., & Lomax, A. (2013). *In vivo* proton range verification: a review. *Phys. Med. Biol.*, **58**, R131–R160.

Koide, A., Kataoka, J., Masuda, T., Mochizuki, S., Taya, T., Sueoka, K., Tagawa, L., Fujieda, K., Maruhashi, T., Kurihara, T., & Inaniwa, T. (2018). Precision imaging of 4.4 MeV gamma rays using a 3-D position sensitive Compton camera. *Sci. Rep.*, **8**(1), 8116.

Krimmer, J., Dauvergne, D., Létang, J. M., & Testa, É. (2018). Prompt-gamma monitoring in hadrontherapy: a review. *Nucl. Instrum. Meth. Phys. Res. A*, **878**, 58–73.

Krimmer, J., Ley, J.-L., Abellan, C., Cachemiche, J.-P., Caponetto, L., Chen, X., Dahoumane, M., Dauvergne, D., Freud, N., Joly, B., Lambert, D., Lestand, L., Létang, J. M., Magne, M., Mathez, H., Maxim, V., Montarou, G., Morel, C., Pinto, M., … Zoccarato, Y. (2015). Development of a Compton camera for medical application based on silicon strip and scintillation detectors. *Nucl. Instrum. Meth. Phys. Res. A*, **787**, 98–101.

Kurosawa, S., Kubo, H., Ueno, K., Kabuki, S., Iwaki, S., Takahashi, M., Taniue, K., Higashi, N., Miuchi, K., Tanimori, T., Kim, D., & Kim, J. (2012). Prompt gamma detection for range verification in proton therapy. *Curr. Appl. Phys.*, **12**(2), 364–368.

Lecoq, P., Morel, C., Prior, J., Visvikis, D., Gundacker, S., Auffray, E., Krizan, P., Turtos, R. M., Thers, D., Charbon, E., Varela, J., de Taille, C. L., Rivetti, A., Breton, D., Pratte, J.-F., Nuyts, J., Surti, S., Vandenberghe, S., Marsden, P., … Benoit, M. (2020). Roadmap toward the 10 ps time-of-flight PET challenge. *Physics in Medicine & Biology.*

Marcatili, S., Collot, J., Curtoni, S., Dauvergne, D., Hostachy, J.-Y., Koumeir, C., Létang, J.-M., Livingstone, J., Metivier, V., Gallin-Martel, L., Gallin-Martel, M.-L., Muraz, J.-F., Servagent, N., Testa, E., & Yamouni, M. (2020). Ultra-fast prompt gamma detection in single proton counting regime for range monitoring in particle therapy. *Phys. Med. Biol.*, **65**(24), 245033.

Maxim, V., Lojacono, X., Hilaire, E., Krimmer, J., Testa, E., Dauvergne, D., Magnin, I., & Prost, R. (2015). Probabilistic models and numerical calculation of system matrix and sensitivity in list-mode MLEM 3D reconstruction of Compton camera images. *Phys. Med. Biol.*, **61**(1), 243–264.

McCleskey, M., Kaye, W., Mackin, S., Beddar, S., He, Z., & Polf, J. C. (2015). Evaluation of a multistage CdZnTe Compton camera for prompt γ imaging for proton therapy. *Nucl. Instrum. Meth. Phys. Res. A*, **785**, 163–169.

Muñoz, E., Barrio, J., Etxebeste, A., Ortega, P. G., Lacasta, C., Oliver, J. F., Solaz, C., & Llosá, G. (2017). Performance evaluation of MACACO: A multilayer Compton camera. *Phys. Med. Biol.*, **62**(18), 7321–7341.

Paganetti, H. (2012). Range uncertainties in proton therapy and the role of Monte Carlo simulations. *Phys. Med. Biol.*, **57**(11), R99–R117.

Parodi, K., & Polf, J. C. (2018). *In vivo* range verification in particle therapy. *Med. Phys.*, **45**(11), e1036–e1050.

Perali, I., Celani, A., Bombelli, L., Fiorini, C., Camera, F., Clementel, E., Henrotin, S., Janssens, G., Prieels, D., Roellinghoff, F., Smeets, J., Stichelbaut, F., & Vander Stappen, F. (2014). Prompt gamma imaging of proton pencil beams at clinical dose rate. *Phys. Med. Biol.*, **59**, 5849–5871.

Richard, M.-H., Chevallier, M., Dauvergne, D., Freud, N., Henriquet, P., Le Foulher, F., Létang, J. M., Montarou, G., Ray, C., Roellinghoff, F., Testa, E., & Walenta, A. H. (2011). Design guidelines for a double scattering Compton camera for prompt-γ imaging during ion beam therapy: A Monte Carlo simulation study. *IEEE Trans. Nucl. Sci.*, **58**(1), 87–94.

Richter, C., Pausch, G., Barczyk, S., Priegnitz, M., Keitz, I., Thiele, J., Smeets, J., Vander Strappen, F., Bombelli, L., Fiorini, C., Hotoiu, L., Perali, I., Prieels, D., Enghardt, W., & Baumann, M. (2016). First clinical application of a prompt gamma based in vivo proton range verification system. *Radiother. Oncol.*, **118**(2), 232–237.

Roellinghoff, F., Benilov, A., Dauvergne, D., Dedes, G., Freud, N., Janssens, G., Krimmer, J., Létang, J. M., Pinto, M., & Prieels, D. (2014). Real-time proton beam range monitoring by means of prompt-gamma detection with a collimated camera. *Phys. Med. Biol.*, **59**(5).

Roellinghoff, F., Richard, M.-H., Chevallier, M., Costanzo, J., Dauvergne, D., Freud, N., Henriquet, P., Le Foulher, F., Létang, J. M., Montarou, G., Ray, C., Testa, E., Testa, M., & Walenta, A. H. (2011). Design of a Compton camera for 3D prompt-γ imaging during ion beam therapy. *Nucl. Instrum. Meth. Phys. Res. A*, **648**, S20–S23.

Rohling, H. M., Priegnitz, M., Schoene, S., Schumann, A., Hueso-González, W. E. E., Pausch, G., & Fiedler, F. (2017). Requirements for a Compton camera for in vivo range verification of proton therapy. *Phys. Med. Biol.*, **62**(7), 2795.

Ros García, A., Barrio, J., Etxebeste, A., García López, J., Jiménez-Ramos, M. C., Lacasta, C., Muñoz, E., Oliver, J. F., Roser, J., & Llosá, J. (2020). MACACO II test-beam with high-energy photons. *Phys. Med. Biol.*, **65**, 245027.

Sarrut, D., Bardiès, M., Boussion, N., Freud, N., Jan, S., Létang, J. M., Loudos, G., Maigne, L., Marcatili, S., Mauxion, T., Papadimitroulas, P., Perrot, Y., Pietrzyk, U., Robert, C., Schaart, D., Visvikis, D., & Buvat, I. (2014). A review of the use and potential of the GATE Monte Carlo code for radiation therapy and dosimetry applications. *Med. Phys.*, **41**(6), 064301.

Schönfelder, V., Himer, A., & Schneider, K. (1973). A telescope for soft gamma ray astronomy. *Nucl. Instrum. Meth.*, **107**(2), 385–394.

Smeets, J., Roellinghoff, F., Prieels, D., Stichelbaut, F., Benilov, A., Busca, P., Fiorini, C., Peloso, R., Basilavecchia, M., Frizzi, T., Dehaes, J. C., & Dubus, A. (2012). Prompt gamma imaging with a slit camera for real-time range control in proton therapy. *Phys. Med. Biol.*, 3371–3405.

Solevi, P., Muñoz, E., Solaz, C., Trovato, M., Dendooven, P., Gillam, J. E., Lacasta, C., Oliver, J. F., Rafecas, M., & Torres-Espallardo, I. (2016). Performance of MACACO Compton telescope for ion-beam therapy monitoring: first test with proton beams. *Phys. Med. Biol.*, **61**, 5149.

Taya, T., Kataoka, J., Kishimoto, A., Iwamoto, Y., Koide, A., Nishio, T., Kabuki, S., & Inaniwa, T. (2016). First demonstration of real-time gamma imaging by using a handheld Compton camera for particle therapy. *Nucl. Instrum. Meth. Phys. Res. A*, **831**, 355–361.

Thirolf, P. G., Aldawood, S., Böhmer, M., Bortfeldt, J., Castelhano, I., Dedes, G., & Fiedler, F. (2016). A Compton camera prototype for prompt gamma medical imaging. *EPJ Web Conf.*, **117**, 05005.

Verburg, J., Hueso-Gonzalez, F., Tattenberg, S., Wohlfahrt, P., Ruggieri, T., & Bortfeld, T. (2020). First-in-human use of prompt gamma-ray spectroscopy for proton range verification. *Joint AAPM/COMP Meeting, July, 2020.*

Xie, Y., Bentefour, E. H., Janssens, G., Smeets, J., Vander Strappen, F., Hotoiu, L., Yin, L., Dolney, D., Avery, S., O'Grady, F., Prieels, D., McDonough, J., Solberg, T. D., Lustig, R. A., Lin, A., & Teo, B.-T. K. (2017). Prompt gamma imaging for in vivo range verification of pencil beam scanning proton therapy. *Int. J. Radiat. Oncol. Biol. Phys.*, **99**(1), 210–218.